Applied Catalysis A: General 470 (2014) 412–419

Contents lists available at ScienceDirect

Applied Catalysis A: General

journal homepage: www.elsevier.com/locate/apcata

# Hierarchically structured Beta zeolites with intercrystal mesopores and the improved catalytic properties

Baoyu Liu, Liming Zheng, Zhihong Zhu, Chao Li, Hongxia Xi*, Yu Qian

*School of Chemistry and Chemical Engineering, South China University of Technology, Guangzhou, Guangdong 510640, PR China*

ARTICLE INFO

*Article history:*
Received 13 August 2013
Received in revised form
11 November 2013
Accepted 13 November 2013
Available online 22 November 2013

*Keywords:*
Hierarchical structure
Heterogeneous catalysis
Surfactant
Beta
DFT

ABSTRACT

Hierarchical Beta zeolite with mesoporous/microporous structure was synthesized by employing a bifunctionalized amphiphilic surfactant. $N_2$ adsorption–desorption isotherms indicated the presence of hierarchical mesopores in this sample. Transmission electron microscopy images confirmed the co-presence of ordered micropores and hierarchical mesopores. This sample exhibited excellent hydrothermal stability. In addition, the prepared hierarchically structured Beta zeolite showed greatly enhanced catalytic activity as compared with conventional counterpart for probe reaction involving large molecules due to the highly mesoporous structure, in which diffusion constraints of reactant molecules are the main concern. Such hierarchical micro/mesostructure Beta zeolite combined good hydrothermal stability and high activities may find potential applications in catalysis and adsorption involving bulky molecules.



## 1. Introduction

Zeolites are a unique class of crystalline aluminosilicates with intricate micropores, which have been widely used as heterogeneous catalysts in petrochemical and fine chemical industries owing to high hydrothermal stability and strong acidity [1,2], as well as in the separation field and environmental field [3,4]. Their superior performance can often be attributed to the existence of a well-defined system of micropores (typically 0.25–1 nm) that enable shape-selective transformations. However, the relatively small and sole micropores in zeolites are often disadvantageous with respect to mass transfer of large molecules because they cause diffusion limitations of reagents and products due to restricted access and slow transport to/from the active site, which results in low catalyst utilization in most industrial reactions catalyzed by zeolites [5,6]. Besides, pore blockage caused by coking is also a severe problem that routinely arises in catalytic applications of zeolites [7].

In past years, researchers have pursued several different preparative strategies in order to synthesize zeolite materials with controlled shapes and porosities to minimize diffusion limitations [8–15]. One promising approach is to integrate multiple levels of porosity by introducing an additional (meso)pore system within an individual zeolite crystal or by making mesoporous frameworks crystallized into zeolites without destroying the mesostructure, which called hierarchically structured zeolites that enable zeolites to have maximum structural functions in a limited space and volume owing to the high diffusion efficiency. The hierarchically structured zeolites possessing mesopores as well as the inherent micropores of zeolite structures are garnering attention as an effective solution to overcome the drawbacks of the diffusion limitation problem of solely microporous classical zeolites. Among them, Möller et al. [14] fabricated hierarchical zeolite Beta nanoparticles using a dense gel steam conversion strategy in a single step, which can be proved a highly efficient method.

Up to date, a number of synthesis strategies have been developed to synthesize such a hierarchical structure [16–21]. Dealumination and desilication [20] were used to achieve mesoporosity involving post-synthesis treatments as a representative non-templating method while most of the synthesis methods known today make use of templates in order to control the generation of mesopores. Among the templating methods, hard template such as carbon blacks [8], carbon nanotubes [22], carbon aerogel [23] and 3DOM carbon [24] has been used to prepare zeolites with desired pore structure as the endo- and exotemplating route. These carbon particles are encapsulated by the zeolite crystals during growth, and then they could be easily removed by calcination to produce highly mesoporous zeolite single crystals. However,

* Corresponding author. Tel.:+86 20 87113501; fax: +86 20 87113735.
*E-mail addresses:* liubaoyu084@163.com (B. Liu), cehxxi@scut.edu.cn (H. Xi).

0926-860X/$ – see front matter. 
http://dx.doi.org/10.1016/j.apcata.2013.11.015

complicated multisteps were usually involved for the dispersion and compatibility of the hard template in the synthesis solution because of the incompatibility between hard substrates and precursor species [25]. In addition, most of generating mesopores in zeolites by the hard template strategy show the characteristic of isolated secondary porosity that are unsuitable for the diffusion of large molecules.

Another method that is distinguished from hard templates is soft templating route. In this approach, surfactant molecules are self-organized into a supramolecular micelle that can be used to synthesize hierarchical zeolites. The micelle is called a soft template duo to the characteristic of flexibility of surfactant micelle during the zeolite synthesis processes. The soft-templating approach has the higher versatility in tailoring the mesoporous structure as compared with the hard-templates mentioned above through the molecular manipulation of functional groups and geometrical packing parameter of the surfactant [26–28]. However, it is difficult for the surfactants to modulate the zeolite crystal growth into a mesoporous structure due to the strong phase-separation tendency between the employed ordinary organic surfactants and the rapidly growing zeolite crystals. Thus a rationally designed surfactant molecule with functional groups is the key to control the interactions between these templates and zeolitic species during crystallization. In this respect, substantial efforts have been made by different groups [29–32]. Among them, the typical ones include cationic or silylated polymer and amphiphilic organosilane. For example, Choi et al. synthesized microporous crystalline molecular sieves with a mesoporous skeleton by using amphiphilic organosilane molecules as a meso-structuring agent in 2006 [10]. Wang et al. used mesoscale cationic polymers such as polymers polydiallyldimethylammonium chloride (PDADMAC) and the dimethyldiallyl ammonium chloride acrylamide copolymer (PDDAM) to prepare the hierarchical mesoporous zeolites [33]. Wang and Pinnavaia prepared MSU-MFI with small intracrystal mesopores (average pore size 2.0–3.0 nm) using a silane-functionalized polyethylenimine as the mesoporogen [11]. Srivastava et al. synthesized nanocrystalline MFI-zeolites with intracrystal mesopores by using alkyltriethoxysilane [31]. Among these studies, an advanced preparation method was proposed by Ryoo's group [34–36] for the preparation of single-unit-cell nanosheets of zeolite and mesoporous molecular sieves by using specially designed surfactant. In 2011, Na and co-workers [36] reported on the synthesis of mesoporous molecular sieves possessing crystalline microporous walls with zeolitelike frameworks using special designed surfactant. In this process, the surfactant played a dual-functional role as both microposity-directing agent and mesoposity-generating template. In a following research, a hierarchical mesopore–micropore Beta zeolite was prepared using various surfactants that can function as a hierarchical structure-directing agent [37]. In our previous work, we prepared a mesoporous ZSM-5 type molecular sieve through a dual-functional surfactant [38].

In the present work, extending the synthesis strategy, a mesoporous/microporous hierarchically structured Beta zeolite was synthesized by employing a single gemini-type tetraquaternary ammonium surfactant, which could generate micropores and mesopores simultaneously. The mesopores were disordered and the zeolite frameworks were highly crystalline, and this material exhibited the high steam stability. The catalytic activity for the esterification reaction of benzyl alcohol with hexanoic involving large organic molecules was tested as a probe reaction using the prepared hierarchically structured Beta zeolites. Results indicated that the hierarchically structured Beta exhibited an improved catalytic performance compared with conventional Beta zeolites featuring only micropores.

## 2. Experimental

### 2.1. Synthesis of organic surfactant

The gemini-type tetraquaternary ammonium surfactant is synthesized according to the literature procedures [36]. In a typical synthesis, first 0.01 mol of 1-Bromohexadecane (98%, J&K) and 0.1 mol of *N*,*N*,*N*′,*N*′-tetramethyl-1,6-hexanediamine (99%, J&K) were dissolved in 50 mL toluene/acetonitrile mixture with v/v = 1:1; then the mixture was refluxed with stirred for 8 h at 65 °C; after cooling to room temperature and solvent evaporation, the precipitated product was $[C_{16}H_{33}–N^{+}(CH_3)_2–C_6H_{12}–N(CH_3)_2][Br^{-}]$. The precipitate was collected by filtration and washed with diethyl ether, and dried in a vacuum oven at 50 °C for 8 h. Second, 0.005 mol $[C_{16}H_{33}–N^{+}(CH_3)_2–C_6H_{12}–N(CH_3)_2][Br^{-}]$and 0.0025 mol α,α′-dichloro-*p*-xylene (98%, J&K) were dissolved in 25 mL of chloroform, which was refluxed with stirred for 12 h at 62 °C. After cooling to room temperature and solvent evaporation, the precipitate was filtered and washed with diethyl ether, and dried in a vacuum oven at 50 °C for 8 h to obtain the final product, the $[C_{16}H_{33}–N^{+}(CH_3)_2–C_6H_{12}–N^{+}(CH_3)_2–CH_2–(p–C_6H_4)–CH_2–N^{+}(CH_3)_2–C_6H_{12}–N^{+}(CH_3)_2–C_{16}H_{33}][Br^{-}]_2[Cl^{-}]_2$ surfactant; it is designated as $Ph(C–N–C_6–N–C_{16})_2$.

### 2.2. Synthesis of the hierarchically structured Beta zeolite

In a typical synthesis, a homogeneously mixed solution was first prepared from tetraethylorthosilicate (TEOS, 98%, J&K), $Ph(C–N–C_6–N–C_{16})_2$ surfactant, $NaAlO_2$ (44.7 wt% $Na_2O$, 52 wt% $Al_2O_3$, J&K), NaOH, ethanol and $H_2O$ with a molar ratio of 3.58 $Na_2O$:16 $SiO_2$:0.4 $Al_2O_3$:0.8 $Ph(C–N–C_6–N–C_{16})_2$ surfactant:128 EtOH:1143 $H_2O$. The resultant gel mixture was aged under magnetic stirring at 65 °C for 12 h. The final gel obtained was transferred into 50 mL Teflon-lined stainless steel autoclave and heated at 150 °C for 5 days. After crystallization, the product was collected by filtration, dried in air, and calcined at 580 °C for 6 h to remove the template. The resulting hierarchically structured Beta zeolite sample is denoted by Beta-H. For comparison, conventional Beta sample was prepared in this study following the literature reports [39], which is denoted by Beta-C.

### 2.3. Characterization

Powder X-ray diffraction (XRD) patterns were recorded on a Rigaku Rotaflex Diffractometer using Cu$K_\alpha$ radiation (λ = 1.5418 Å). Scanning electron microscopy (SEM) images were recorded on a JSM-6330F electron microscope at an acceleration voltage of 10 kV. Transmission electron microscopy (TEM) images were obtained with a JEM-2100HR electron microscope operated at 200 kV. The FTIR spectra of samples in the form of KBr pellets were recorded at room temperature on a Bruker Vector 33-IR spectrometer with a resolution of 1 $cm^{-1}$. The thermal behavior of a washed, as-synthesized sample was followed on a Perkin-Elmer Pyris 6 TGA analyzer with a heating rate of 5 °C/min under a nitrogen flow of 30 mL/min. $N_2$ adsorption–desorption isotherms were measured with a Micromeritics ASAP 2020 system at 77 K. The samples were outgassed for 12 h at 150 °C before the measurements. The specific surface areas of materials were calculated from the adsorption branch of the isotherm using the Brunauer–Emmett–Teller (BET) equation, and the pore-size distribution was analyzed by using the Barrett–Joyner–Halenda (BJH) method. $^{27}Al$ MAS NMR spectra were recorded on a Bruker Avance AV 400 spectrometer at 104.26 MHz. A saturated aqueous aluminum sulfate solution with a chemical shift 0.0 ppm was used as an external reference. $NH_3$–TPD was performed on a homemade apparatus; 50 mg powder sample was placed in a quartz tubular reactor and heated at a rate of

10 °C/min to 550 °C for 120 min under He flow. After the temperature cooled down to room temperature in $N_2$ flow, the sample was exposed to $NH_3$ for the sufficient adsorption, and then the weakly adsorbed $NH_3$ was removed by flowing He for 2 h at 120 °C. Desorption profile was then recorded with a rate of 10 °C/min using a gas chromatography equipped with a TCD detector. Pyridine adsorption experiments were performed on self-supported wafers in an IR cell. Before the IR measurements, each sample was degassed at 500 °C for 2 h in a vacuum, and then pyridine was adsorbed on the degassed sample wafer for 1 h at room temperature. The system was then evacuated at different temperatures, and IR spectra were collected using a Bruker Vector 33-IR spectrometer with 2 $cm^{-1}$ resolution in the 4000–400 $cm^{-1}$ range.

### 2.4. Calculations

The density functional theory (DFT) with a hybrid functional B3LYP level at the 6-31G* basis set was adopted to calculate the properties of the title surfactant. This basis set provided accurate geometry and electronic properties for a wide range of organic compounds [40,41]. All the calculations were performed using Gaussian 03W program package. In addition, molecular electrostatic potential (MEP) and frontier molecular orbitals were determined at the same level of theory B3LYP/6-31G* with the optimized structure.

### 2.5. Catalytic reaction

Before the catalytic tests, all the samples were ion-exchanged three times with 1 M $NH_4NO_3$ solution at 90 °C and then converted to the $H^+$ form via calcination in flowing nitrogen (120 mL/min) at 550 °C for 6 h. The esterification reaction of benzyl alcohol and hexanoic acid was carried out under nitrogen atmosphere using a three-necked flask equipped with a reflux condenser. In a typical reaction, toluene (12 mL), benzyl alcohol (15 mmol), hexanoic acid (18 mmol) and catalyst (0.2 g) were mixed with continuous stirring and the reaction was conducted at 110 °C for 3 and 6 h, respectively. After the reaction, reaction mixture was centrifuged and analyzed by a GC-MS (QP2010) and Waters HPLC system (UV detection wavelength was set at 257 nm).

## 3. Results and discussion

### 3.1. Characterization of the hierarchically structured Beta zeolite

Fig. 1 shows the X-ray diffraction (XRD) patterns of Beta-H and Beta-C samples. All samples exhibited the characteristic Bragg reflections corresponding to the *BEA zeolite structure, which proved the formation of the Beta zeolite crystals. Comparing the Beta-C sample with the Beta-H samples reveals that the diffraction pattern of the Beta-C has a higher intensity than that of Beta-H samples. This could be attributed to the lower effect of the $Ph(C–N–C_6–N–C_{16})_2$ surfactant as a structure directing agent than traditional tetraethylammonium ions ($TEA^+$) template [42]. In addition, no significant difference is observed in the intensity and positions of these peaks in both as-synthesized and calcined Beta-H samples from the Fig. 1, which indicates that crystalline zeolite frameworks of Beta-H sample were not destroyed at high temperature atmosphere.

IR spectra (Fig. 2) provided evidence for the formation of Beta units in the Beta-H sample. Two structural vibrational bands are observed at 400–500 $cm^{-1}$, which are Si–O bending modes observed in all amorphous $SiO_2$ materials [43]. However, the Beta-C sample exhibits a distinct vibration at 520–600 $cm^{-1}$; these bands could be ascribed to the five- and six-member rings of T–O–T (T = Si or Al) in the structure of zeolite Beta [44]; such vibration is also

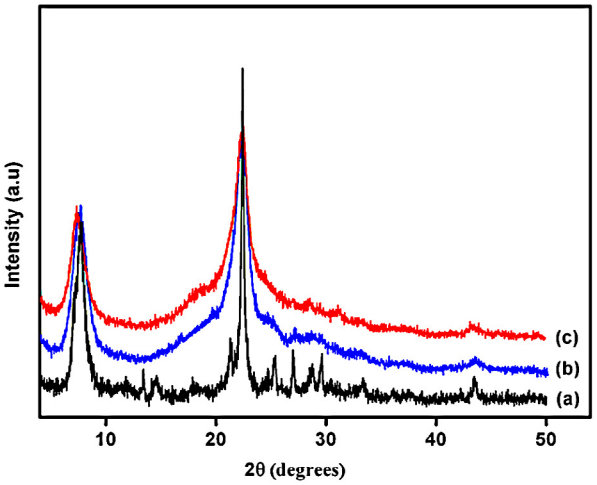


**Fig. 1.** Wide-angle XRD patterns of (a) pure Beta zeolite, (b) as-synthesized Beta-H and (c) calcined Beta-H at 580 °C.

detected in the spectrum of Beta-H sample, indicating that the Beta-H sample contains the primary units of zeolite Beta. In addition, a band is observed about 620 $cm^{-1}$ only in the sample Beta-C, which is evidence for a higher extent of zeolitization [45].

The nitrogen adsorption and desorption isotherms and mesopore size distributions in Fig. 3 illustrate the differences in porosity between Beta-C and Beta-H samples. The nitrogen sorption isotherms show a high uptake at the very initial stage, in all of the samples, indicating the presence of micropores in zeolites. The major difference of Beta-H isotherm from that of Beta-C is a distinct increase of $N_2$ adsorption in the region $0.6 < P/P_0 < 0.9$ (Fig. 3a), which is caused by the capillary condensation in the textural mesopores. The broad hysteresis loop in Beta-H sample indicates the presence of hierarchical mesopores. The mesoporosity for the Beta-H derivatives originates from the templating effect of the $Ph(C–N–C_6–N–C_{16})_2$ surfactant. Correspondingly, the Barrett–Joyner–Halenda (BJH) model was used to estimate the mesopore size distributions of Beta-H and Beta-C samples. The result exhibits mesopores in the range 2.5–30 nm, centered at 3.4 nm for Beta-H sample (Fig. 3b). In contrast, the Beta-C sample does not contain any mesopores and the hysteresis loop. A more detailed analysis (Table 1) reveals that both mesopore

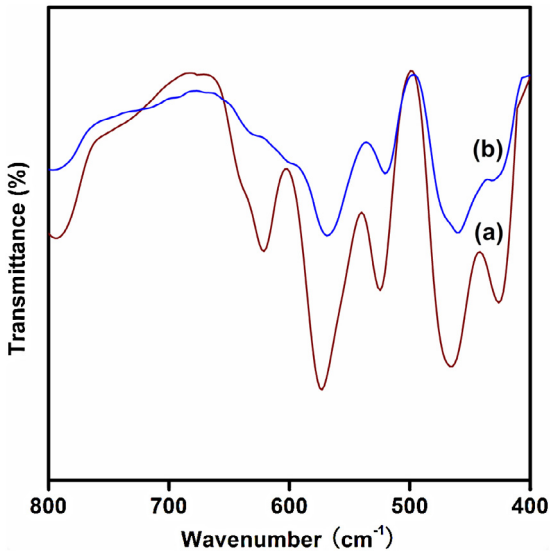


**Fig. 2.** IR spectra of calcined samples: (a) Beta-C and (b) Beta-H.

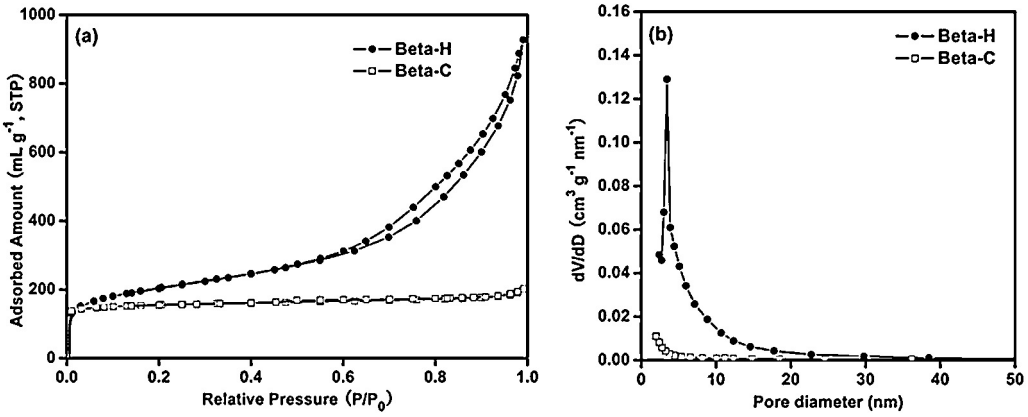


**Fig. 3.** (a) Nitrogen adsorption/desorption isotherms of Beta-C and Beta-H; (b) pore size distributions of Beta-C and Beta-H.

**Table 1**
Textual properties of the selected samples.

| Sample | Si/Al[a] | $S_{BET}$[b] ($m^2\ g^{-1}$) | $S_{ext}$[c] ($m^2\ g^{-1}$) | $S_{mic}$[c] ($m^2\ g^{-1}$) | $V_{tol}$[c] ($cm^3\ g^{-1}$) | $V_{ext}$[d] ($cm^3\ g^{-1}$) | $V_{mic}$[c] ($cm^3\ g^{-1}$) |
|---|---|---|---|---|---|---|---|
| Beta-C | 16 | 520 | 107 | 413 | 0.30 | 0.11 | 0.19 |
| Beta-H | 14 | 803 | 627 | 176 | 0.89 | 0.74 | 0.15 |
| Beta-H[e] | 17 | 765 | 587 | 178 | 0.78 | 0.66 | 0.12 |

[a] Si/Al ratio was obtained by ICP/AES analysis.
[b] $S_{BET}$ is the specific BET surface area obtained from $N_2$ adsorption.
[c] Micropore and external surface areas and micropore volumes by *t*-plot method.
[d] Total pore volumes are obtained at $P/P_0 = 0.95$.
[e] 40% steam treatment at 800 °C for 12 h.

volume (0.74 $cm^3$/g) and external surface area (627 $m^2\ g^{-1}$) of Beta-H sample are larger than those of Beta-C sample (0.11 $cm^3$/g) and (107 $m^2\ g^{-1}$), respectively. All of the above results confirm the generation of mesoporosity in Beta-H sample. The possibility of maintaining a hierarchical structure is attractive for catalytic applications involving large molecules.

Fig. 4a shows scanning electron microscopy (SEM) image of Beta-H sample. Zeolite particles with relatively uniformed

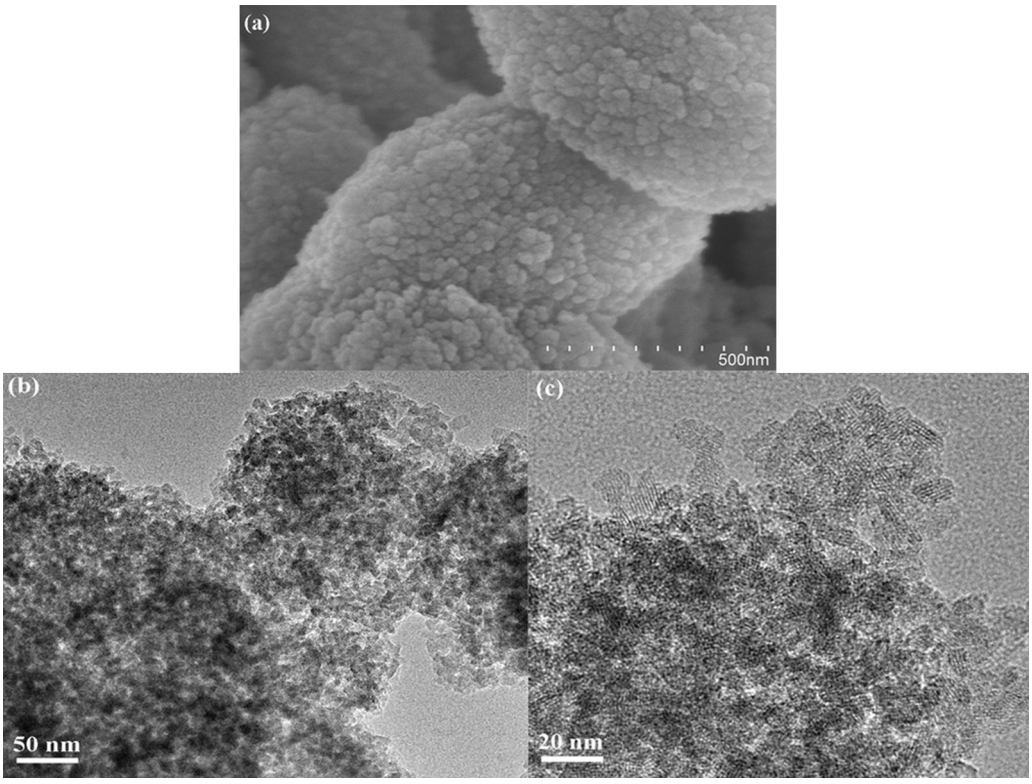


**Fig. 4.** Electron microscopes of Beta-H samples: (a) SEM image of Beta-H and (b, c) TEM images of Beta-H at different magnifications.

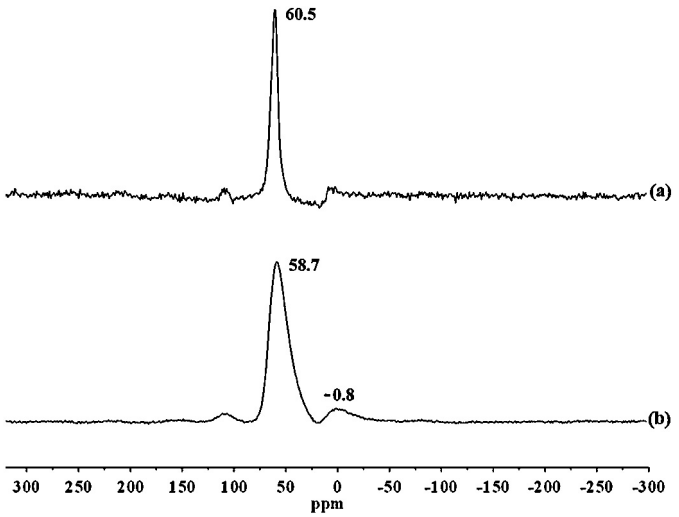


**Fig. 5.** $^{27}$Al MAS NMR spectra of (a) as-synthesized Beta-H and (b) calcined Beta-H at 580 °C.

nanocrystals in size and morphology were observed. No physically isolated crystals or particles of the two phases were detected throughout the entire sample. The SEM image exhibits agglomeration of particles with a rough surface of hierarchical zeolites, which indicates that the surfactant could protect zeolite nanocrystal surfaces from further growth. High-resolution transmission electron microscopy (TEM) provides insight into the local structure of crystalline phases. Fig. 4b shows the TEM image of Beta-H sample, which exhibits both disordered hierarchical mesopores and ordered micropores, in agreement with nitrogen sorption results. Furthermore, the lattice fringe can be clearly seen in the high-resolution TEM (HR-TEM) image of the sample (Fig. 4c), which indicates that the entire particle is crystalline with mesopores penetrating through the micropore framework. As a result, high thermal stability and strong acidity can be expected. These results confirm the co-presence of ordered micropores and hierarchical mesoporosity in Beta-H sample; such a hierarchical arrangement in Beta-H is important for mass transport.

The acidity of the samples is related to the environment of Al atoms located in frameworks. The tetracoordinated Al site becomes a Brønsted acid via $H^+$ ion that can be located on the bridging oxygen between Si and Al, such as Si–$OH^+$–Al; the acid strength varies according to the Si–O–Al angle and the presence of other framework Al atoms in the vicinity [46]. The structural configuration and the location of Al atoms were investigated by $^{27}$Al MAS NMR spectroscopy (Fig. 5). The sharp, symmetrical signal is centered at about $\delta$ = 60.5 ppm for as-synthesized sample (Fig. 5a), which corresponds to tetrahedral aluminum species. The absence of a peak at 0 ppm in as-synthesized sample demonstrates that Al is entirely incorporated in the framework. A slight broadening of the peak ($\delta$ = 58.7) can be observed for the calcined sample (Fig. 5b), and the intensity of the peak of tetrahedrally coordinated aluminum decreases in comparison with the as-synthesized sample. Besides, there is a small peak at 0.8 ppm in the calcined sample, indicating that a small fraction (< 9.6%) of the Al atoms was separated from the framework and transformed into octahedral Al. It is a common phenomenon for aluminosilicates materials to form octahedral Al during calcination.

Thermogravimetric analysis (TGA) of as-synthesized Beta-H sample is presented in Fig. 6a. The weight loss up to 120 °C is attributed to physically adsorbed water in the porous material. The weight loss at higher temperature ranges of 160–280 °C, 280–420 °C and 420–700 °C is assigned reasonably to the decomposition of cationic surfactant in the sample. The larger weight loss (25%) in as-synthesized Beta-H sample indicates that the occluded surfactant could be removed by burning, which led to the large pore volume and complex porosity in Beta-H sample [33].

The IR spectra of pyridine adsorbed on protonated sample of Beta-H in the 1700–1400 $cm^{-1}$ is shown in Fig. 6b. The sample exhibited band at 1596 $cm^{-1}$ due to the hydrogen-bonded pyridine [47]. The bands at 1445 and 1490 $cm^{-1}$ could be attributed to C=C vibration of aromatic type from the ring of pyridine, which are related to adsorption of the pyridine molecule on Lewis-type acid sites [48]. Moreover, the band at 1545 $cm^{-1}$ is characteristic of the Brønsted acid sites [49]. It is obvious that the relative intensities of the bands for Brønsted acid sites and Lewis acid sites decreased at the two thermal desorption temperatures, and it is not capable of withstanding temperatures up to 400 °C, indicating the moderate acid sites strength.

Hydrothermal stability of Beta-H sample was evaluated by exposing the calcined sample to 40% water vapor at 800 °C for 12 h. Fig. 7a illustrates the X-ray diffraction (XRD) patterns of calcined Beta-H before and after exposure to 40% water vapor. After the steam treatment, the intensity of Bragg reflections decreased to some extent, which indicated that the steam treatment resulted in the slight the destruction of microporous frameworks and it was responsible for reduction of the crystallinity. $N_2$ isotherm of Beta-H treated in 40% steaming (Fig. 7b) showed a similar nitrogen isotherm and pore-size distribution to the untreated sample (Fig. 3). The sample showed a BET surface area loss of only about 5% (Table 1). Fig. 7c illustrates the $^{27}$Al MAS NMR spectra of calcined Beta-H before and after steam treatment. From

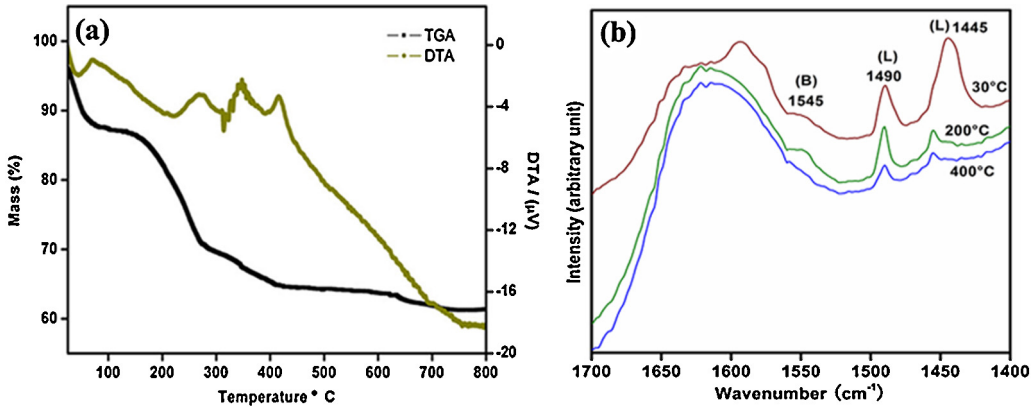


**Fig. 6.** (a) Thermogravimetric (TG) and Differential thermal analysis (DTA) curves of as-synthesized Beta-H; (b) IR spectra of pyridine absorbed on Beta-H samples at different temperatures. Lewis acid sites (L) and Brønsted acid sites (B) are marked.

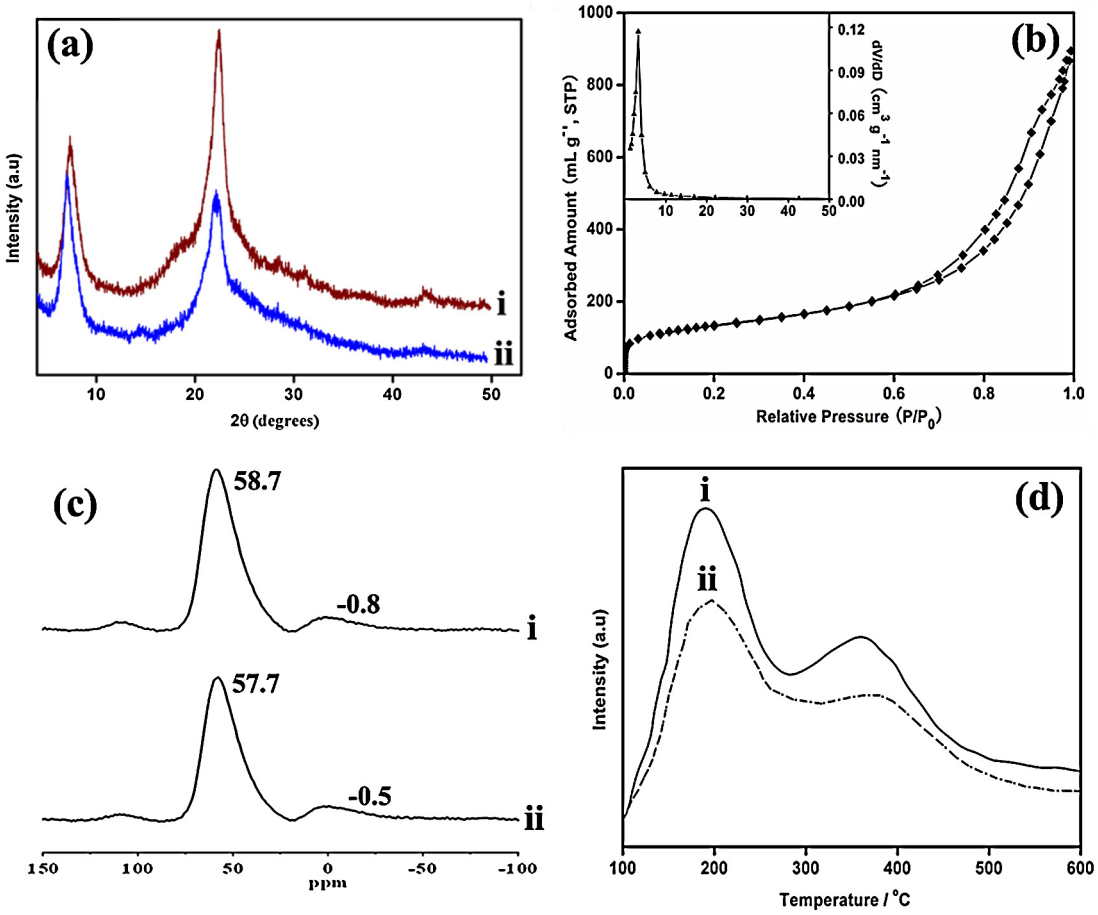


**Fig. 7.** (a) Wide-angle XRD patterns, (c) $^{27}$Al MAS NMR spectra and (d) $NH_3$–TPD curves of calcined Beta-H before (i) and after (ii) 40% steam treatment at 800 °C for 10 h. (b) $N_2$ isotherms and pore-size distributions on calcined Beta-H after 40% steam treatment at 800 °C for 10 h.

Fig. 7c, it can be clearly seen that the chemical shift for the tetrahedral aluminum sites was lower in steam-treated sample (57.7 ppm) than in raw sample (58.7 ppm), and the chemical shift for the extra-framework octahedral aluminum sites was larger in steam-treated sample (−0.5 ppm) than in raw sample (−0.8 ppm), which indicated that a small fraction of the Al atoms was separated from the framework and transformed into octahedral Al during the steam treatment, but transformed proportion of octahedral Al species in steam-treatment process was very low. Fig. 7d shows temperature-programmed desorption of ammonia ($NH_3$–TPD) curves on calcined Beta-H before and after steam treatment. It can be seen that before and after steam-treated Beta-H samples exhibited both the low-temperature peak at about 200 °C for weak acid sites and the high-temperature broad peak at about 370 °C for medium acid sites, and the curve shape of steam-treated sample was very similar to that of raw sample, indicating that the acidic strength and amount of steam-treated sample were similar to those of raw Beta-H zeolite. The present results support that Beta-H sample possesses high steam stability, which is a crucial factor for its applications in a wide range of industrial processes and reactions.

### 3.2. Computational study

The $Ph(C–N–C_6–N–C_{16})_2$ surfactant used in the present work contained hydrophilic multi-quaternary ammonium groups and hydrophobic alkyl chain moiety. Such a cationic amphiphilic surfactant could easily disperse into synthesis solution and strongly interact with the negatively charged silica species through the formation of covalent bonds with other $SiO_2$ and $Al_2O_3$ sources during the crystallization of zeolites. Such a strong interaction of the surfactant and aluminosilicate species and its effective structure-directing ability to Beta zeolite may be attributed to its polyquaternary ammoniums molecular structure. Herein, molecular electrostatic potential (MEP) was calculated based on optimized geometry (Fig. 8a). MEP image (Fig. 8b) shows that the positive

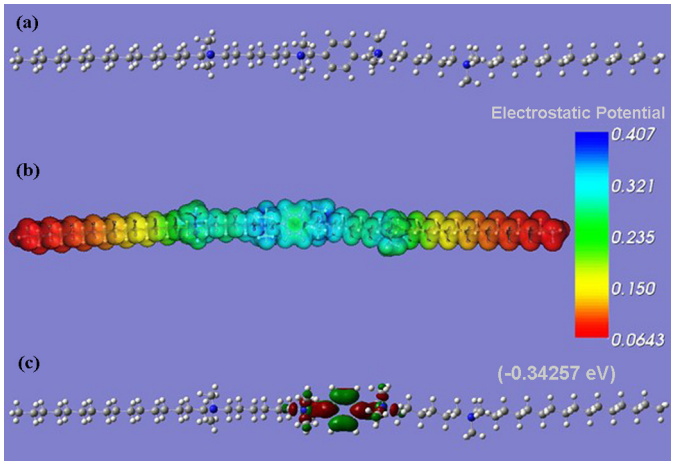


**Fig. 8.** (a) Optimized structure, (b) molecular electrostatic potential map and (c) molecular orbital surfaces and energy levels of the 'Bifunctional' cationic surfactant (atom legend: white = H; gray = C; blue = N). (For interpretation of the references to color in this figure legend, the reader is referred to the web version of this article.)

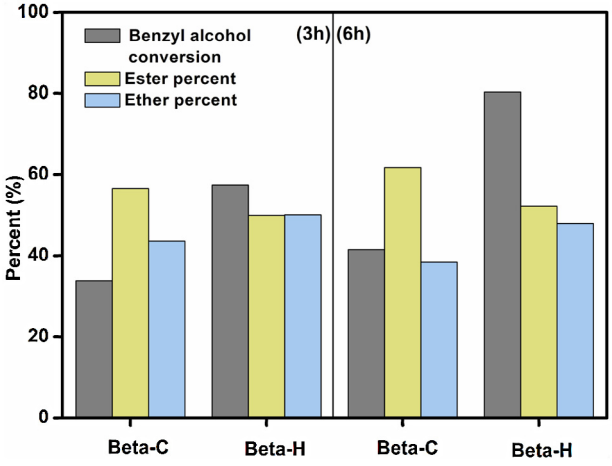


**Fig. 9.** Catalytic activity of Beta-H and Beta-C in the esterification reaction of benzyl alcohol and hexanoic acid.

regions are mainly over ammonium groups, especially on the inner ammonium groups linked with the benzene ring. Fig. 8c shows the distributions of LUMO (the lowest unoccupied molecular orbital) for the cationic surfactant. The LUMO is directly related to the electron affinity and characterizes the susceptibility of the molecule toward attack by nucleophiles. The lower the values of LUMO are, the stronger the electron accepting abilities of the molecules. As can be seen from Fig. 8c, the LUMO is mainly located on benzene ring and adjacent two ammonium groups, which indicates that the inner ammonium groups could be the most susceptible sites for nucleophilic attacks and could interact with anionic aluminosilicate species.

The bifunctionalized amphiphilic surfactant not employed as mesoporogen, but act as an effective structure-directing agent for the Beta zeolite in the microscale. Based on the strong interactions between the zeolite precursor and bifunctionalized surfactant by covalent bonding or electrostatic forces estimated by DFT calculations, the hierarchically structured Beta zeolites discussed above could be synthesized. The polyquaternary ammonium groups acted as an effective structure-directing agent for the Beta zeolite, while the hydrophobic interaction between the hydrophobic alkyl chain groups induced the formation of mesoscale structure, which was attributed to the effect of growth interruption of zeolite crystals owing to the adsorption of surfactant on the crystal surface of Beta. Notably, the inner ammonium groups may have more contribution as the zeolite-structure-directing function, which is in agreement with the Jung et al.'s [50] experiment results that demonstrated that the gemini-type surfactants containing only the tailed ammoniums were unable to generate zeolite frameworks at all.

### 3.3. Catalytic activity

The esterification reaction of benzyl alcohol and hexanoic acid was chosen as a probe reaction to investigate the effect of the facile diffusion in the hierarchically structured Beta zeolite on catalytic performance, in which bulk molecular species were involved. At the beginning in 3 h, the Beta-H and Beta-C samples gave 57% and 33% conversion of benzyl alcohol, respectively. The ester selectivity was 56% and 49% respectively (Fig. 9). Significantly higher conversions of benzyl alcohol have been achieved on Beta-H (80%) than on Beta-C (41%) after reactions for 6 h. The Beta-H exhibited superior catalytic activities above conventional Beta with the conversion of benzyl alcohol of Beta-H being two times that of Beta-C, which should be directly assigned to the contribution of mesopores in hierarchically structured Beta zeolites owing to the high accessibility of large reactant molecules in mesopores [25]. Notably, the ester selectivity over Beta-C is slightly higher than that of Beta-H, indicating that the conventional Beta may inhibit the dehydrative condensation between two alcohol molecules due to the sole presence of micropores. However, both the Beta-H and Beta-C exhibited lower ester selectivity than previous hierarchical MFI and conventional MFI zeolites, respectively [30], which could be attributed to the structure difference between *BEA and MFI.

Apparently, the hierarchically structured Beta zeolite of the present study has the merit for catalytic applications in large molecular reactions. Nevertheless, further work would be necessary for other catalytic reactions. However, the micropores are indeed much more accessible due to significantly improved mass transport in the hierarchically structured Beta zeolite compared with conventional Beta zeolite; thus it is reasonable that improved catalytic performance of hierarchical porous zeolite structures has been attributed to enhanced transport. Furthermore, the hierarchically structured Beta zeolite shows great potential as an industrial catalyst, and can be extended to various fields such as adsorption and separation technologies.

## 4. Conclusion

In summary, a hierarchically structured Beta zeolite has been successfully synthesized by using a bifunctionalized amphiphilic surfactant. A detailed investigation showed that the resultant zeolite products have a well-connected, disordered intercrystal mesoporosity. The $Ph(C–N–C_6–N–C_{16})_2$ surfactant played a dual-functional role as both structure-directing agent for the Beta zeolite and mesoporosity-generating template during the crystal growth. It is proposed that the multi-ammonium head groups could interact with zeolite precursor as an effective structure-directing agent, while the hydrophobic interaction between the long-chain tails induced the formation of a mesoscale micellar structure. This sample exhibited excellent hydrothermal stability and high catalytic activity for conversion of bulky substrates that cannot enter zeolite micropores. Such a hierarchical micro/mesoporous structure is useful to its applications in various fields such as catalysis, adsorption and separation. Further work would be necessary for the generalization of this method to other kinds of zeolites and the resistance to deactivation properties to other catalytic reactions. More studies are in progress in our laboratory.

## Acknowledgments

This work was supported by the National Natural Science Foundation of China (Nos. 20936001 and 21176084), the National High Technology Research and Development Program of China (No. 2013AA065005) and Guangdong Natural Science Foundation (S2011 030001366).

## References

[1] C.S. Cundy, P.A. Cox, Chem. Rev. 103 (2003) 663–702.
[2] A. Corma, Chem. Rev. 97 (1997) 2373–2420.
[3] M. Stöcker, Microporous Mesoporous Mater. 82 (2005) 257–292.
[4] J. Choi, G. Ghosh, Z.-P. Lai, M. Tsapatsis, Angew. Chem. Int. Ed. 45 (2006) 1154–1158.
[5] J.-H. Kim, T. Kunieda, M. Niwa, J. Catal. 173 (1998) 433–439.
[6] K. Beschmann, L. Riekert, U. Müller, J. Catal. 145 (1994) 243–245.
[7] G. Caeiro, R.H. Carvalho, X. Wang, M.A.N.D.A. Lemos, F. Lemos, M. Guisnet, F. Ramôa Ribeiro, J. Mol. Catal. A: Chem. 255 (2006) 131–158.
[8] C.J.H. Jacobsen, C. Madsen, J. Houzvicka, I. Schmidt, A. Carlsson, J. Am. Chem. Soc. 122 (2000) 7116–7117.
[9] Y. Tao, H. Kanoh, K. Kaneko, J. Am. Chem. Soc. 125 (2003) 6044–6045.
[10] M.K. Choi, H.S. Cho, R. Srivastava, C. Venkatesan, D.-H. Chi, R. Ryoo, Nat. Mater. 5 (2006) 718–723.
[11] H. Wang, T.J. Pinnavaia, Angew. Chem. Int. Ed. 45 (2006) 7603–7606.

[12] W. Fu, L. Zhang, T. Tang, Q. Ke, S. Wang, J. Hu, G. Fang, J. Li, F.-S. Xiao, J. Am. Chem. Soc. 133 (2011) 15346–15349.
[13] Y. Sun, R. Prins, Angew. Chem. Int. Ed. 47 (2008) 8478–8481.
[14] K. Möller, B. Yilmaz, R.M. Jacubinas, J. Am. Chem. Soc. 133 (2011) 5284–5295.
[15] F.N. Gu, F. Wei, J.Y. Yang, N. Lin, W.G. Lin, Y. Wang, H. Zhu, Chem. Mater. 22 (2010) 2442–2450.
[16] F.-S. Xiao, L.F. Wang, C.Y. Yin, K.F. Lin, Y. Di, J.X. Li, R.R. Xu, D.S. Su, R. Schlögl, T. Yokoi, T. Tatsumi, Angew. Chem. Int. Ed. 45 (2006) 3090–3093.
[17] W. Fan, M.A. Snyder, S. Kumar, P.S. Soolee, W.C. Yoo, A.V. Mccormick, R.L. Penn, A. Stein, M. Tsapatsis, Nat. Mater. 7 (2008) 984–991.
[18] Y. Fang, H. Hu, J. Am. Chem. Soc. 128 (2006) 10636–10637.
[19] C.J.H. Jacobsen, C. Madsen, J. Houzvicka, I. Schmidt, A. Carlsson, J. Am. Chem. Soc. 122 (2000) 7116–7117.
[20] J.C. Groen, J.A. Moulijn, J. Perez-Ramirez, J. Mater. Chem. 16 (2006) 2121–2131.
[21] J.C. Groen, T. Bach, U. Ziese, A. Donk, K.P. de Jong, J.A. Moulijn, J. Perez-Ramirez, J. Am. Chem. Soc. 127 (2005) 10792–10793.
[22] I. Schmidt, A. Boisen, E. Gustavsson, K. Ståhl, S. Pehrson, S. Dahl, A. Carlsson, C.J.H. Jacobsen, Chem. Mater. 13 (2001) 4416–4418.
[23] Y. Tao, H. Kanoh, K. Kaneko, J. Phys. Chem. B 107 (2003) 10974–10976.
[24] H. Chen, J. Wydra, X. Zhang, P.-S. Lee, Z. Wang, W. Fan, M. Tsapatsis, J. Am. Chem. Soc. 133 (2011) 12390–12393.
[25] J. Zhou, Z. Hua, Z. Liu, W. Wu, Y. Zhu, J. Shi, ACS Catal. 1 (2011) 287–291.
[26] J.S. Beck, J.C. Vartuli, W.J. Roth, M.E. Leonowicz, C.T. Kresge, K.D. Schmitt, C.T-W. Chu, D.H. Olson, E.W. Sheppard, S.B. McCullen, J.B. Higgins, J.L. Schlenker, J. Am. Chem. Soc. 114 (1992) 10834–10843.
[27] D. Zhao, Q. Huo, J. Feng, B.F. Chmelka, G.D. Stucky, J. Am. Chem. Soc. 120 (1998) 6024–6036.
[28] J.Y. Ying, C.P. Mehnert, M.S. Wong, Angew. Chem. Int. Ed. 38 (1999) 56–77.
[29] W.-C. Li, A.-H. Lu, R. Palkovits, W. Schmidt, B. Spliethoff, F. Schüth, J. Am. Chem. Soc. 127 (2005) 12595–12600.
[30] R. Srivastava, M. Choi, R. Ryoo, Chem. Commun. (2006) 4489–4491.
[31] R. Srivastava, N. Iwasa, S.-I. Fujita, M. Arai, Chem. Eur. J. 14 (2008) 9507–9511.
[32] F. Liu, T. Willhammar, L. Wang, L. Zhu, Q. Sun, X. Meng, W. Carrillo-Cabrera, X. Zou, F.-Z. Xiao, J. Am. Chem. Soc. 134 (2012) 4557–4560.
[33] L. Wang, Z. Zhang, C. Yin, Z. Shan, F.-S. Xiao, Microporous Mesoporous Mater. 131 (2010) 58–67.
[34] M. Choi, K. Na, J. Kim, Y. Sakamoto, O. Terasaki, R. Ryoo, Nature. 461 (2009) 246–249.
[35] K. Na, M. Choi, W. Park, Y. Sakamoto, O. Terasaki, R. Ryoo, J. Am. Chem. Soc. 132 (2010) 4169–4177.
[36] K. Na, C. Jo, J. Kim, K. Cho, J. Jung, Y. Seo, R.J. Messinger, B.F. Chmelka, R. Ryoo, Science 333 (2011) 328–332.
[37] K. Cho, K. Na, J. Kim, O. Terasaki, R. Ryoo, Chem. Mater. 24 (2012) 2733–2738.
[38] B.Y. Liu, C. Li, Y.Q. Ren, Y.Z. Tan, H.X. Xi, Y. Qian, Chem. Eur. J. 210 (2012) 96–102.
[39] M.A. Camblor, A. Mifsud, J. Pérez-Pariente, Zeolites 11 (1991) 792–797.
[40] B.Y. Liu, Z. Liu, G.C. Han, Y.H. Li, Thin Solid Films 519 (2011) 7836–7844.
[41] J.H. Henríquez-Román, M. Sancy, M.A. Páez, L. Padilla-Campos, J.H. Zagal, C.M. Rangel, G.E. Thompson, J. Solid State Electrochem. 9 (2005) 504–511.
[42] Y. Liu, W. Zhang, T.J. Pinnavaia, Angew. Chem. Int. Ed. 40 (2001) 1255–1258.
[43] J.C. Jansen, F.J. van der Gaag, H. van Bekkum, Zeolites 4 (1984) 369–372.
[44] Z.T. Zhang, Y. Han, F.S. Xiao, S.L. Qiu, L. Zhu, R.W. Wang, Y. Yu, Z. Zhang, B.S. Zou, Y.Q. Wang, H.P. Sun, D.Y. Zhao, Y. Wei, J. Am. Chem. Soc. 123 (2001) 5014–5021.
[45] Y. Xia, R. Mokaya, J. Mater. Chem. 14 (2004) 863–870.
[46] Y. Seo, K. Cho, Y. Jung, R. Ryoo, ACS Catal. 3 (2013) 713–720.
[47] Y.S. Ooi, R. Zakaria, A.R. Mohamed, S. Bhatia, Appl. Catal., A 274 (2004) 15–23.
[48] P. Morales-Pacheco, F. Alvarez, L. Bucio, J.M. Domínguez, J. Phys. Chem. C 113 (2009) 2247–2255.
[49] K. Kim, R. Ryoo, H.D. Jang, M. Choi, J. Catal. 288 (2012) 115–123.
[50] J. Jung, C. Jo, K. Cho, R. Ryoo, J. Mater. Chem. 22 (2012) 4637–4640.